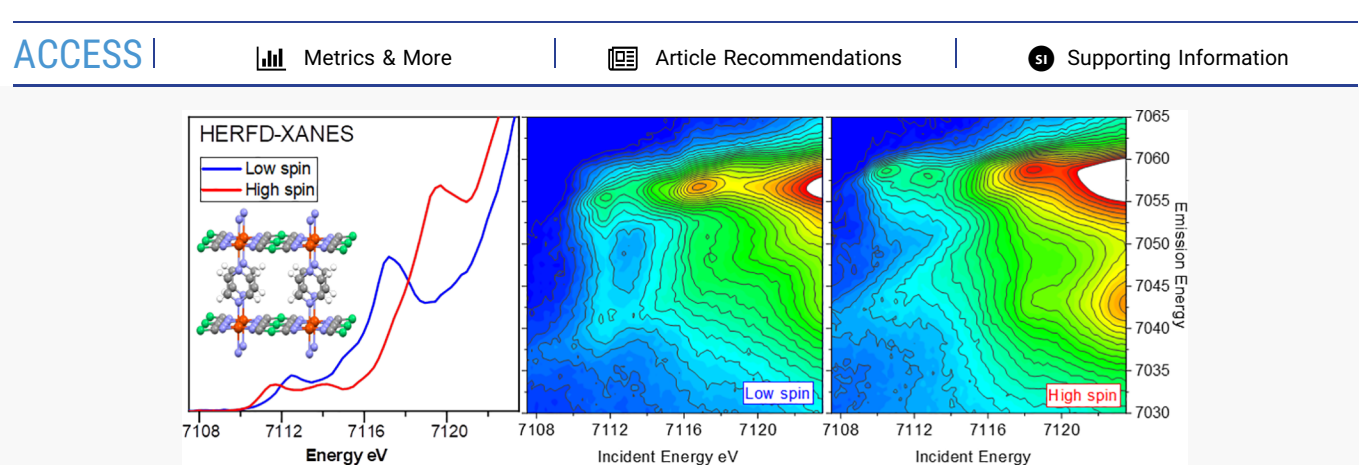
Inorganic Chemistry

pubs.acs.org/IC Article

Local Coordination and Electronic Structure Ramifications of Guest-Dependent Spin Crossover in a Metal—Organic Framework: A Combined X-ray Absorption and Emission Spectroscopy Study

Mikhail Solovyev, Pavel Kucheryavy, and Jenny V. Lockard*





ABSTRACT: The porous Hoffman-type 3D lattice $Fe(pz)[Ni^{II}(CN)_4]$ exhibits thermally induced spin-crossover (SCO) behavior that is dependent on the solvent guest species occupying the pores. Here, in situ Fe K-edge X-ray absorption spectroscopy (XAS) and both non-resonant and resonant $K\beta$ X-ray emission spectroscopy (XES) methods are used to probe this framework under two solvent environments that yield different extremes of spin crossover temperature: acetonitrile and toluene. While the acetonitrile pore environment engenders an SCO response around room temperature, toluene guests stabilize the high spin state and effectively suppress SCO behavior throughout the ambient temperature range. The multipronged X-ray spectroscopy approach simultaneously confirmed this spin crossover behavior and provided new local coordination and electronic structural insights of the framework under these two solvent environments. Extended X-ray absorption fine structure analysis revealed spin state and solvent guest-dependent differences in coordination bond lengths and structural disorder. Resonant XES measurements produced high-resolution XAS spectra with distinct pre-edge and edge features, whose assignment was established using both simple ligand field theory and time-dependent density-functional theory calculations and further supported by their observed resonance behavior in the 2D RXES plane. Edge feature variation with the Fe spin state was interpreted to reveal changes in specific metal-linker bond covalency.

INTRODUCTION

The rational design of multifunctional nanoscale materials for switching, sensing, and memory device applications depends on the capacity to engineer them with controlled response to external stimuli. With permanent porosity and tunable chemical composition for selective host-guest interactions, metal-organic frameworks (MOFs) or porous coordination polymers (CPs) that also display spin-crossover (SCO) phenomena upon external perturbation have emerged as promising candidates in this field. 1-3 MOFs are composed of metal ions or clusters that self-assemble with organic molecular linkers to form three-dimensional (3D) porous networks. The pore dimensions, chemical functionality, and electronic structure of these crystalline materials can be tuned by varying the metal/linker composition and stoichiometry. Their permanent microporosity creates large surface areas that were initially targeted for various adsorption-based applications, such as gas separation and storage, catalysis, and chemical sensing. $^{4-9}$ The tunability of MOF structure and composition has also been recognized as an opportunity to impart specific electronic and magnetic properties, including the promotion of guest-dependent SCO behavior to produce spin-switchable porous lattices. $^{10-21}$

Among the most well-studied spin-crossover frameworks (SCOFs) are a set of Hofmann-type 3D lattices with the general formula $Fe^{II}(pz)[M^{II}(CN)_4]$, composed of Fe(II) tetracyanometallate layers (where $M^{II}=Ni$, Pd or Pt)

Received: March 8, 2022 Published: June 9, 2022





connected through apically coordinated pyrazine (pz) linkers.^{3,15–26} Like other SCO systems,^{27–33} the octahedral ligand field-induced d-orbital splitting energy of the open shell d⁶ Fe sites is close to the electron pairing energy. This engenders parallel stability of the low-spin (LS) and high-spin (HS) states and a propensity to switch between the two in response to external stimuli (e.g., temperature or light). Furthermore, the 3D pillared-layer porous framework creates an environment where the spin-transition temperature can vary over a large range up to room temperature and exhibit thermal hysteresis behavior, depending on the adsorbed guest species. 15,18-20,22 The pronounced guest dependence of the SCO behavior is attributed to both the relatively small pore dimensions (~7.2 Å) and the differences in adsorbed guest interactions with the framework host. 15,16,34 Guest species with strong framework interactions that lead to restricted pz linker ring rotation tend to stabilize the LS state due to the loss of entropy and therefore increase the observed SCO temperature. However, larger guests that are significantly constrained within the confined pores are found to have the opposite effect and shift the spin-transition temperature to, in some cases, far lower values. These sterically hindered guests may restrict the pz rotation, but they also severely hamper the contraction of the Fe-N first shell coordination distances, and this tends to stabilize the HS state. Reported experimental and computational studies of these materials have primarily focused on the guest interactions with the pz linkers of the framework, providing a detailed account of the molecular-level origins for the observed SCO trends. 16,17,24,25,34,35 However, the local geometric and electronic structure changes of the Fe sites themselves (i.e., the components actually undergoing the spin transitions) have not been probed at the same level. Variable temperature magnetic susceptibility measurements clearly established the overall SCO behavior and in situ diffraction studies tracked the corresponding long-range structure changes in these SCOFs, ¹⁹ yet these measurements do not fully capture local electronic and structural changes associated with spin transition at the Fe sites. Mossbauer spectroscopy is a valuable tool for studying Fe-based SCO systems, 33,36-39 but isotopic labeling, cryogenic temperatures, and/or very long data acquisition times are often required to produce the data quality needed for deeper electronic structure insight beyond spin state assignment, particularly for lower-concentration Fe samples.

Here, we use element-specific X-ray spectroscopy methods to probe the Fe sites within this type of SCOF in more detail. Through conventional X-ray absorption spectroscopy (XAS), extended X-ray absorption fine structure (EXAFS) analysis verifies local coordination environment changes associated with the spin transition, including Fe-L bond lengths previously established through crystallographic means, along with the extent of guest-dependent local disorder. Fe K β X-ray emission spectroscopy (XES) is a sensitive Fe spin state probe and therefore a useful complementary method for tracking spin transitions in SCOFs. 40 Furthermore, $K\beta$ emission collected under resonance conditions, that is, over an incident X-ray energy range spanning the K absorption edge, can provide new insight on the local electronic structure of the Fe sites beyond a simple spin state assignment. Selecting specific, narrow-range emission slices from the resulting two-dimensional (2D) RXES planes affords high-resolution XAS spectra with pre-edge and edge features that are otherwise poorly resolved or obscured in conventional X-ray absorption near-edge structure (XANES)

analysis. 41-44 Resonance behavior of these features observed in the 2D RXES planes can aid their assignment as long as the effects of core-hole lifetime and other broadening phenomena are taken into account. While still underutilized compared to conventional XAS spectroscopy, this type of RXES analysis applied to other transition metal-based complexes and materials^{45–53} demonstrates its capacity for measuring the SCOF system presented here. Upon assignment, the XAS-edge feature behavior can reveal changes in specific metal-linker bond covalency associated with the spin-dependent fluctuations in the Fe coordination environment. While other X-ray spectroscopy methods, namely, ligand K-edge and metal Ledge XAS, can have stronger sensitivity to metal-ligand bond covalency, 54-59 these soft X-ray techniques (for nitrogenous ligands and first-row transition metals) are generally unsuitable for investigating host-guest materials due to saturation effects, a lower threshold for X-ray damage, and their incompatibility with the required high-vacuum sample conditions. The hard Xray K β RXES method applied to the iron-based SCOF materials in this study avoids these issues and provides dual insights on both metal spin and bond covalency.

In this work, we investigate the $Fe^{II}(pz)[Ni^{II} (CN)_4]$ version²² of the SCOF series described above. Two different solvent guest environments that yield drastically different SCO properties, as previously reported, 19 are explored: acetonitrile and toluene for comparison. Acetonitrile, with suspected strong interactions with the pz linkers as a guest, stabilizes the LS state, producing an SCO response around room temperature, while toluene, as a bulky guest molecule, stabilizes the HS state and effectively suppresses the SCO behavior across the entire ambient temperature range measured. The ramifications of the thermally induced spin-transition behavior in this SCOF are probed in situ using the X-ray spectroscopy methods described above. Analysis of the RXES data is supplemented by time-dependent density-functional theory (TD-DFT) calculations to aid assignment and interpretation of the observed XAS spectral features.

MATERIALS AND METHODS

Materials. Fe(BF₄)₂ 6·H₂O (97%) was purchased from Aldrich, pyrazine ($C_4H_4N_2$) (98%) and $K_2Ni(CN_4)$ were purchased from Alfa Aesar, and MeOH was purchased from Sigma-Aldrich, and they were used without further purification.

MOF Synthesis. The SCO Fe^{II}(pz)[Ni^{II}(CN)₄]-based SCOF was prepared according to a modified literature procedure. 19 The reaction was run on a 0.250 mmol scale with all reactants dissolved in the following solvent mixtures: Fe(BF₄)₂ in 20 mL of a 1:1 mixture of MeOH/H₂O, pyrazine in 20 mL of MeOH and K₂Ni(CN₄) in 20 mL of H₂O. Each reactant solution was subsequently degassed via three freeze-pump-thaw cycles. The pyrazine solution was added dropwise to the Fe(BF₄)₂ solution over a period of 5 min, after which the K2Ni(CN4) solution was added dropwise over a period of 10-15 min. The reaction mixture was then stirred under nitrogen gas for 24 h. The resulting orange powder precipitate was isolated and characterized with powder X-ray diffraction (PXRD) (Figure S1) to confirm crystallinity and phase. Samples of the SCOF were subsequently activated under vacuum at 150 °C for a period of 18 h and soaked in either toluene (Tol) or acetonitrile (Acn) over a period of 24-48 h to introduce the different solvent guest environments. The resulting frameworks, SCOF-Tol and SCOF-Acn, were isolated via vacuum filtration and characterized via PXRD (see the Supporting Information).

X-ray Spectroscopy. Both X-ray absorption (XAS) and emission (XES) measurements were collected simultaneously at the 20ID beamline of the Advanced Photon Source. The X-ray beam was

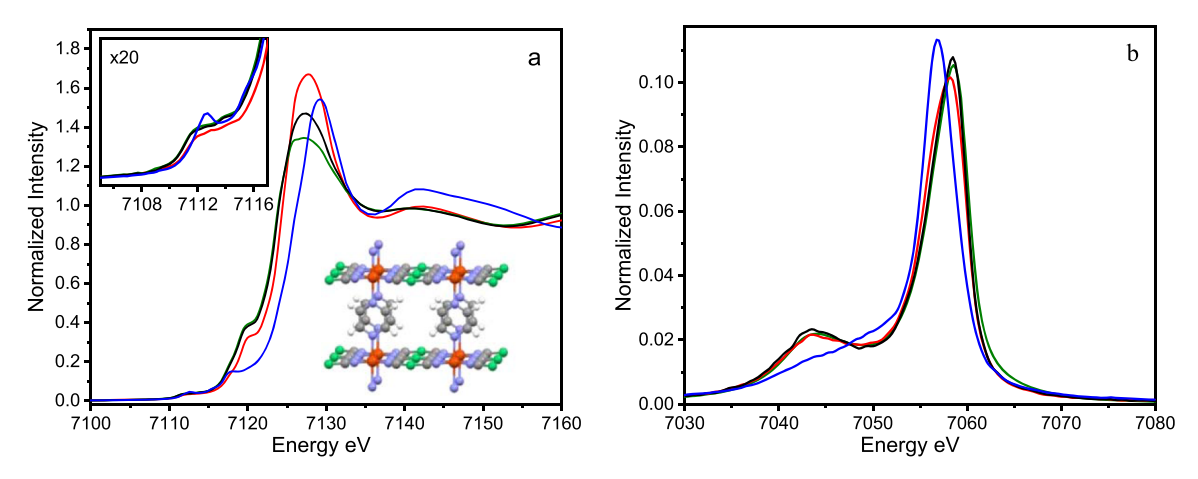


Figure 1. Fe K-edge (a) conventional XANES with the SCOF structure at the bottom right and (b) non-resonant Kβ XES of SCOF-Tol-HT (green), SCOF-Tol-LT (black), SCOF-Acn-LT (blue), and SCOF-Acn-HT (red).

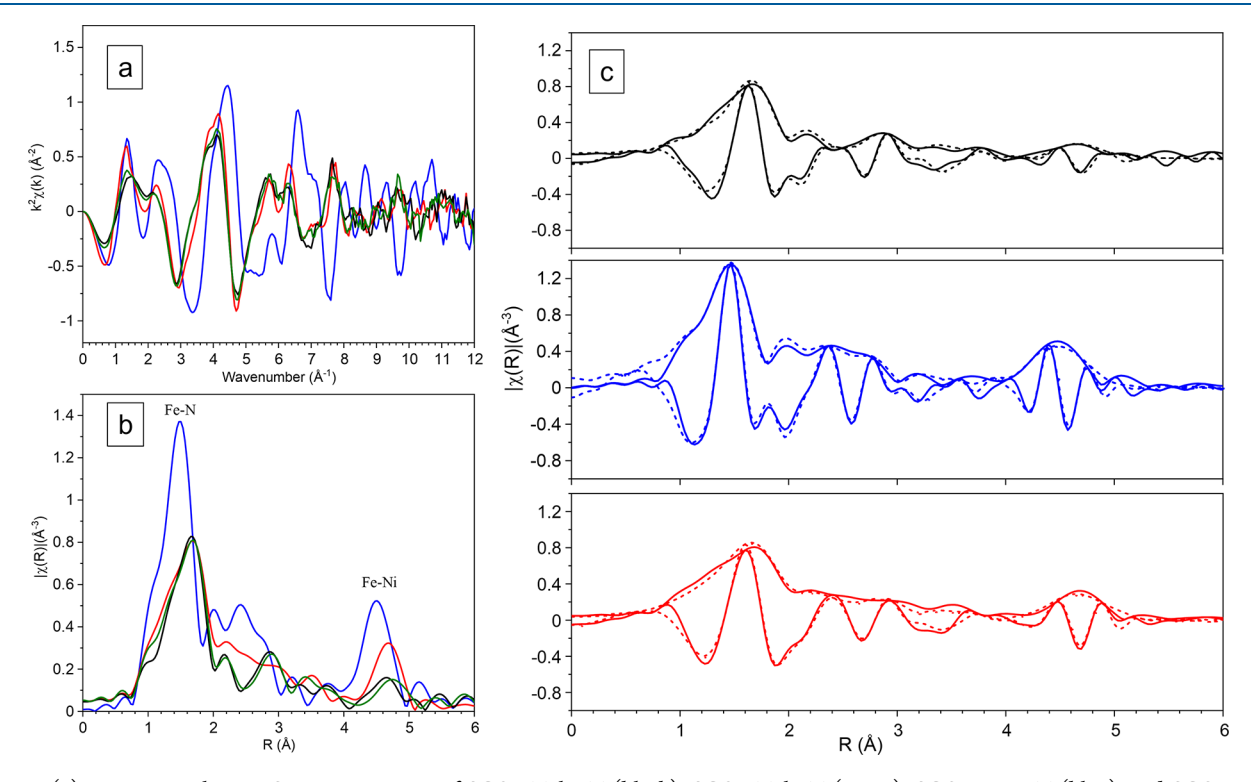


Figure 2. (a) Experimental EXAFS K-space spectra of SCOF-Tol-HT (black), SCOF-Tol-LT (green), SCOF-Acn-LT (blue), and SCO-Acn-HT (red). (b) Experimental EXAFS R-space spectra, identical labels of K-space with regions corresponding to Fe—N and Fe—Ni paths labeled. (c) EXAFS spectra fits (dashed lines) to experimental (solid lines) with magnitude and real components depicted of SCOF-Tol-HT (top, black), SCOF-Acn-LT (middle, blue), and SCO-Acn-HT (bottom, red).

monochromatized using a Si(111) monochromator. Thoroughly ground, undiluted samples were packed in 1.5 mm Kapton tubes and were heat-sealed prior to measurements. The samples were mounted to a copper block sample holder setup with an incorporated thermocouple temperature probe and water flow lines connected to a Neslab RTE-140 refrigerated bath/circulator for in situ temperature control of the sample. After stability studies, sample damage prevention was achieved using the following measures: (a) defocusing X-ray beam to a spot size of 50 \times 50 μ m, (b) detuning the beam by 15%, (c) shuttering the beam during each monochromator move, and (d) linearly translating sample by 50 μ m after each scan. The SCOF samples were measured simultaneously by XES and transmission mode XAS at two temperature extremes between 13 and 54 °C and monitored for temperature stability for at least an hour.

X-ray Absorption Spectroscopy. XAS data were collected at the Fe (7111.2 eV) and Ni (8333.0 eV) K-edges in the transmission mode.

 I_0 , I_v and $I_{\rm r}$ were measured in 30 cm ionization chambers, each with 100% N₂ gas composition. Fe and Ni metal foils were used for incident X-ray energy calibration (7111.2 eV for Fe and 8333.0 for Ni). An average of 3 scans was used to produce each reported XAS spectrum. EXAFS fitting was performed using the Artemis software package. Details of the fitting model are included in the Results and Supporting Information sections.

X-ray Emission Spectroscopy. Resonant and non-resonant Fe K β X-ray emission data were collected using a miniXES spectrometer equipped with Ge(620) crystals and a Pilatus 100 K detector. Fe metal foil was used for incident energy calibration (7111.2 eV). The emission energy window was calibrated using elastic scattering peaks measured over this energy range (7005–7115 eV) and had a point density of 0.2 eV. Fe K β emission spectra were collected with 0.5 s acquisition time for each spectrum over the incident X-ray energy range of 7050.75–8080.75 eV, averaged over 50–60 spectra, and used

to produce 2D incident versus emission energy plots (RXES planes) as well as incident energy versus energy transfer plots (RIXS planes). Three incident energy slices, centered around the highest intensity of the K $\beta_{1,3}$ peak, were selected for each sample and binned to generate high-energy resolution fluorescence detected (HERFD)–XANES spectra. Non-resonant Fe K β emission spectra were acquired by binning XES spectral slices over the incident X-ray energy range of 7700–8000 eV.

TD-DFT calculations. XAS calculations were performed using the TD-DFT approach implemented in the ORCA 3.02 package.⁶² The computational models used for the iron centers, which contained two pyrazine ligands in axial positions and four nitrogen-bound cyanide ligands in equatorial positions, were derived from the experimental crystal structures of the SCOF in the LS and HS states.¹⁹ Calculations were performed using the PBE0 functional,⁶³ a split basis set consisting of TZVP(-f)⁶⁴ for all atoms except iron, which used the CP(PPP) basis set,⁶⁵ zeroth-order regular approximation,⁶⁶ and a conductor-like screening model (COSMO).⁶⁷ For simulation of XANES spectra, the first 30 roots were selected and transitions were restricted to those originating from the Fe 1s orbital. Simulated spectra were generated using 1.5 eV Gaussian broadening. Calculated orbitals were visualized and rendered using the Avogadro software package.

RESULTS

X-ray Absorption Spectroscopy. XANES. Conventional Fe K-edge XANES spectra for SCOF-Tol and SCOF-Acn, collected at both high- and low-temperature extremes are plotted in Figure 1a. Conventional Ni XANES spectra were also collected and are plotted in the Supporting Information (Figure S2). The edge energies, as derived from the first derivative spectra (Figure S3), are found at 7123.4 eV for both SCOF-Tol-HT and SCOF-Tol-LT, 7124.1 eV for SCOF-Acn-HT, and 7125.5 eV for SCOF-Acn-LT. SCOF-Tol-HT, SCOF-Tol-LT, and SCOF-Acn-HT (HT and LT standing for high temperature and low temperature, respectively) all display similar spectra containing a poorly resolved split pre-edge feature with maxima around 7112 and 7114 eV and an edge feature around 7119 eV. As expected, only the acetonitrile guest environment yields a temperature-induced spectral change. Upon temperature reduction from 54 to 13 °C, the rising edge and white line of SCOF-Acn shifts to a higher energy by ~1.5 eV, the edge feature shifts to a lower energy by ~2 eV, going from ~7119 to ~7117 eV, and the pre-edge features converge to a single peak with a maximum around 7112.5 eV. Notably, since samples were optimized for XES measurements, we likely observe some self-absorption saturation effects resulting in suppressed white line intensity, particularly for the SCOF-Tol sample. However, our analysis focuses exclusively on the XANES pre-edge and edge features, which are negligibly affected by the white line attenuation.

EXAFS. Experimental EXAFS spectra for SCOF-Acn-HT, SCOF-Acn-LT, and SCOF-Tol-HT are overlaid in Figure 2a,b. Qualitatively, SCOF-Acn-HT and SCOF-Tol-HT display amplitude-suppressed first shell peaks shifted to higher *R* values compared to that of SCOF-Acn-LT. The EXAFS fitting results are summarized in Tables S1 and S2 and shown in *R*-space in Figure 2c. The fit was performed in *R*-space over 1–5 Å using a *k*-range of 2–12 Å⁻¹ with an arbitrary *k*-weight of 2 for the Fourier transform spectra. The fitting models for both HS and LS structures were derived from their respective crystal structures, ¹⁹ and each contained the same set of fitting parameters. Full fitting parameter definitions are included in the Supporting Information section along with an illustration of the model used to define the scattering paths.

Briefly, the models include equatorial plane Fe-N, Fe-C, and Fe-Ni single scattering paths with distance variables dependent on a heavily restrained CN bond length variable and fixed degeneracies defined by the crystal structure. Several multiple scattering paths within this equatorial plane are included in the fits since the forward focusing effects arising from the linear atomic arrangement of the cyano groups lead to substantial amplitude contributions. These scattering paths are defined using variables dependent on the single-scattering path components. The model also incorporates separate first and second shell scattering paths involving the axially coordinated pyrazine rings. These include a doubly degenerate Fe-N_{pz} single scattering path defined by an independent distance variable and Fe-C_{pz} scattering paths with distance variables dependent on an independent ring distortion parameter, φ , and the associated trigonometric bond length and angle relationships. φ primarily accounts for the out-of-plane distortion of the pyrazine ring convoluted with any small bond length changes within the ring itself as the individual contributions of these two types of ring distortion would be indistinguishable.

X-ray Emission Spectroscopy. *Non-Resonant XES.* Non-resonant $K\beta$ XES data for SCOF-Tol and SCOF-Acn, collected at both high and low temperatures, are shown in Figure 1b and summarized in Table 1. The spectrum of SCOF-Tol contains

Table 1. Summary of Non-Resonant XES Data Collected for SCOF-Acn and SCOF-Tol a

SCOF	spin state	Kß′ (eV)	Kß _{1,3} (eV)	$\frac{\Delta E}{(\mathrm{eV})}$	IKß'/IKß _{1,3}
SCOF-Acn-LT	LS	7043.5	7056.8	13.3	0.111
SCOF-Acn-HT	HS	7043.8	7058.2	14.4	0.194
SCOF-Tol-LT	HS	7044	7058.4	14.4	0.206
SCOF-Tol-HT	HS	7044	7058.4	14.4	0.206

^aPeak energies and intensity ratios determined by pseudo-Voigt curve fits to experimental data.

two prominent features, $K\beta'$ and $K\beta_{1,3}$, positioned around 7044 and 7058 eV, respectively. The toluene guest environment again elicits no temperature-dependent response over the range measured, with both SCOF-Tol-HT and SCOF-Tol-LT exhibiting nearly identical spectra. SCOF-Acn displays a similar XES spectrum but only at elevated temperature. Drastic yet reversible (Figure S4) differences are observed upon temperature decrease from 54 to 13 °C for the acetonitrile guest environment. The spectral evolution accompanying the transition from SCOF-Acn-HT to SCOF-Acn-LT involves significant reduction of the $K\beta'/K\beta_{1,3}$ peak intensity ratio and energy splitting.

RXES. Fe $K\beta$ RXES planes collected for SCOF-Acn-HT, SCOF-Acn-LT, and SCOF-Tol-HT are depicted by the 2D color maps shown in Figure 3. HERFD—XANES spectra (shown in Figures 4 and S6) were extracted from these RXES data by binning three constant emission energy (CEE) slices around the $K\beta_{1,3}$ peak maximum for each sample. These high-resolution spectra present far more detail of the edge and preedge features compared to the conventional XANES. Spectra for SCOF-Tol-HT and SCOF-Acn-HT are nearly identical and display two pre-edge features at 7111.7 and 7114.2 eV as well as a prominent edge feature at 7119.7 eV. The HERFD—XANES spectrum of SCOF-Acn-LT displays a single pre-edge

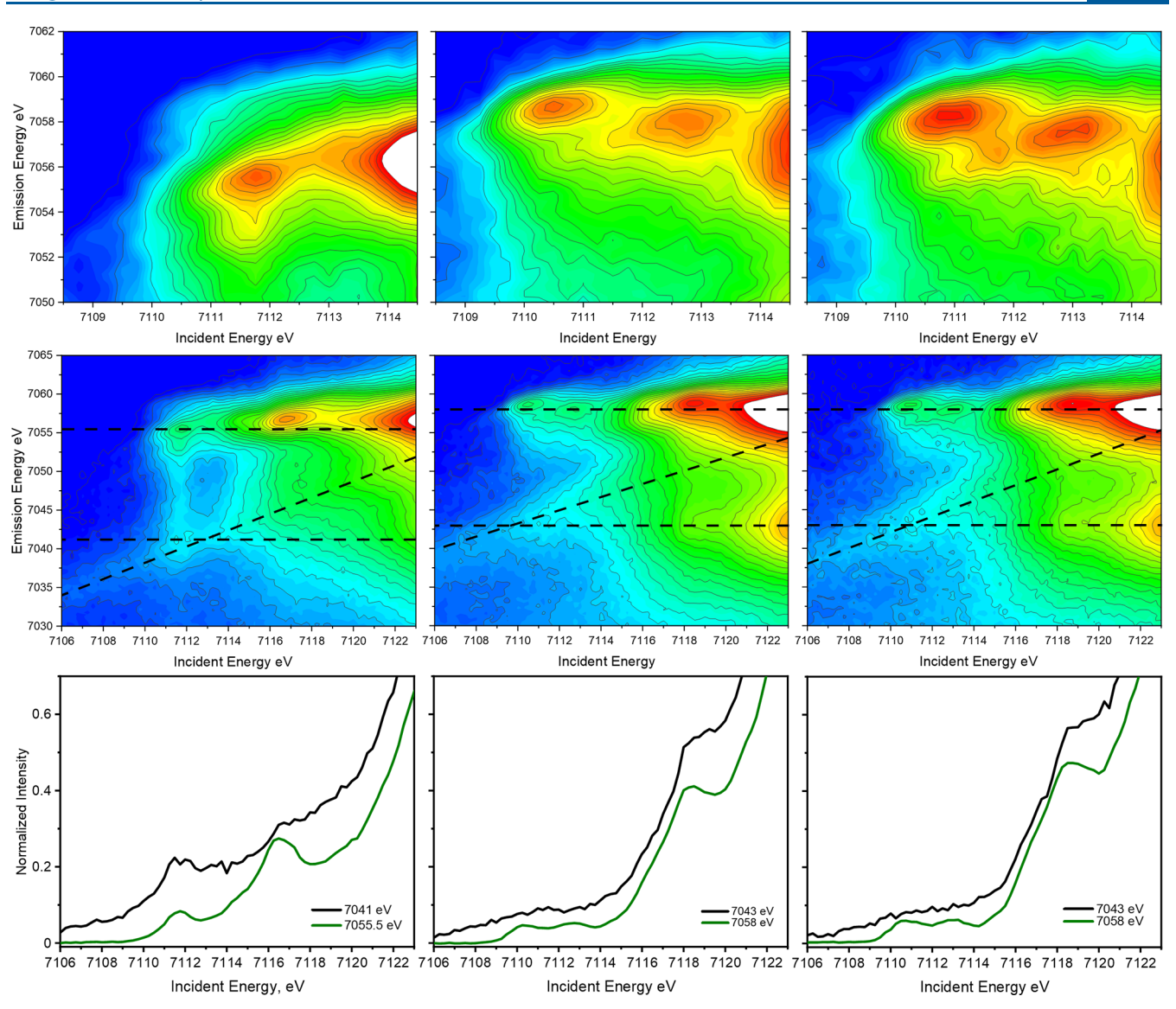


Figure 3. Normalized RXES contour plots for (a) SCOF-Acn-LT, (b) SCOF-Acn-HT, and (c) SCOF-Tol-LT. Top: linear contour plots focusing on the pre-edge region in resonance with the $K\beta_{1,3}$ emission line. Middle: log scale contour plots expanded to include pre-edge and edge feature resonances with both $K\beta_{1,3}$ and $K\beta'$ emission lines. Bottom: comparison of $K\beta_{1,3}$ and $K\beta'$ CEE slices for each of the species.

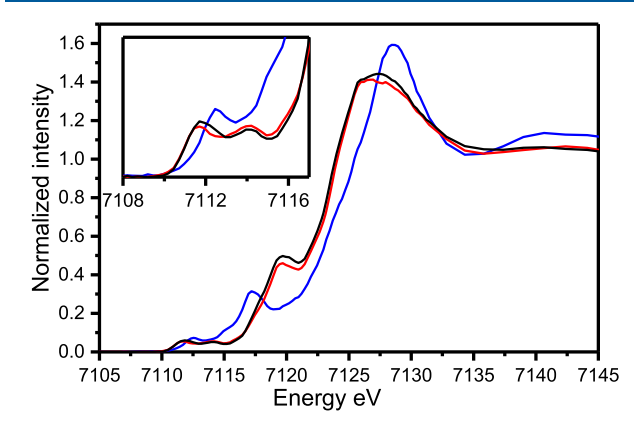


Figure 4. HERFD—XANES spectra for SCO-Tol (Black), SCO-Acn-LT (Blue), and SCO-Acn-HT (Red). Inset: magnified pre-edge region of these HERFD—XANED spectra.

feature at 7112.5 eV and a principal edge feature at 7117.2 eV with a shoulder at 7114.9 eV.

Evaluation of the full RXES plane reveals the resonance behavior of these pre-edge and edge features as well as their confluence with different broadening elements. The CEE slices extracted along the $K\beta_{1,3}$ and $K\beta'$ emission lines are shown in Figure 3 (bottom). The $K\beta_{1,3}$ CEE slices for all three systems contain resonance peaks at the corresponding absorption preedge and edge feature energies. Notably, however, only SCOF-Acn-LT displays the pre-edge peak resonance along the $K\beta'$ CEE slice. Higher-energy edge feature resonances are exposed by the $K\beta'$ CEE slices as well, but broadening effects that occur in the same energy range complicate the assignment as will be discussed below.

Plotting these RXES data as incident versus energy transfer planes, Figure S8, better reveals the effect of core-hole lifetime broadening mechanisms. In this energy perspective, intermediate state broadening ($\Gamma_{\rm int}$) associated with 1s electron excitation and final state broadening ($\Gamma_{\rm fin}$) associated with subsequent 3p to 1s decay occur in purely horizontal and vertical directions, respectively. The effect of the "Raman-like" $\Gamma_{\rm int}$ broadening (which occurs along the diagonal direction in

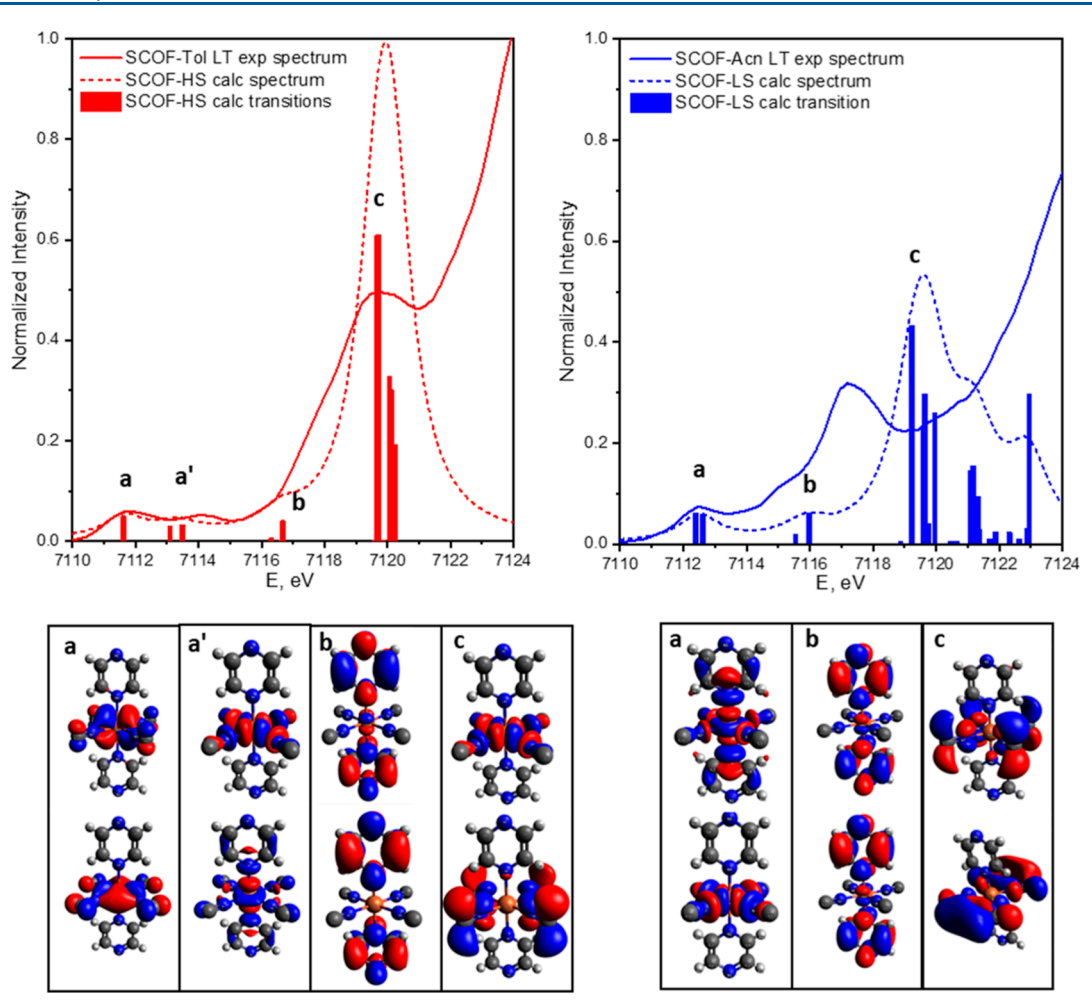


Figure 5. Comparison of the experimental HERFD-XANES (solid line) and calculated spectra (dashed line and sticks) for the SCOF system with LS (right) and HS (left) Fe centers. The relevant acceptor orbitals are depicted below each set of spectra to illustrate the dominant orbital parentage of the different pre-edge and edge feature transitions (labeled a-c).

the incident vs emission energy spectra) is most prevalent at the white line energy-transfer resonance, 71 eV for SCOF-Acn-LT and 67 eV for both SCOF-Acn-HT and SCOF-Tol. Broadening along these energy transfer lines extends into the edge and pre-edge resonance energy ranges, leading to a background that at least partially obscures the resonance features in this region of the RXES plane. This overlap is particularly pronounced in the edge feature energy region (~7116 eV) of the SCOF-Acn-LT system.

TD-DFT Calculations. The calculated XAS spectra with 1.5 eV simulated broadening and underlying transitions for the SCOF with low and HS ground states are overlaid with the corresponding experimental HERFD-XANES spectra in Figure 5. The dominant orbital contributions to the highest oscillator strength pre-edge and edge transitions are shown below each set of spectra. A full list of calculated transitions is provided in the Supporting Information. The LS state structure yields calculated transitions at 7112.3 and 7112.6 eV that, with broadening, contribute to a single pre-edge feature around this energy. The HS state system begets multiple calculated transitions grouped around 7111.6 and 7113.2 eV, resulting in a split pre-edge feature in this energy range when broadening is included. Higher energy edge transitions are calculated as well for the two spin states, with an intermediate energy transition around 7116 eV and a cluster of transitions with a strong oscillator strength around 7120 eV for both systems.

After applying the same fixed energy shift (17.35 eV) to both spectra, the calculated $1s \rightarrow 3d$ pre-edge features reasonably align with those observed experimentally. The edge features revealed in the HERFD–XANES spectra are reproduced computationally as well, although with lower energy accuracy as expected given that the method implemented in ORCA is not optimized for calculating transitions with significant charge-transfer (CT) character such as these. Despite this deviation in calculated energy, particularly the LS system, the relative intensities and general trend in edge feature energy with the spin state are preserved. Furthermore, these calculations provide the first evidence for the assignment of these features based on their associated orbital parentage as discussed below.

DISCUSSION

Guest-Dependent, Thermally Induced SCO Behavior: Confirmation and the Corresponding Structural Ramifications. X-ray spectroscopy characterization of these SCOFs confirms their expected spin state status under different temperature/guest environment conditions. Thanks to the exchange interaction between the 3p core hole and the partially filled 3d orbitals in the final state, the resulting two mainline

features of $K\beta$ X-ray emission spectra, $K\beta_{1,3}$ and $K\beta'$, exhibit energy splitting and intensity ratio sensitivity to the number of unpaired electrons and therefore the spin state of the absorbing metal. The non-resonant XES comparison shown in Figure 1 clearly indicates the HS status of the SCOF-Tol regardless of temperature, while the shift of the $K\beta_{1,3}$ peak to a lower energy and a decrease in intensity of the $K\beta'$ peak indicate a thermally induced HS to LS conversion for SCOF-Acn with reduced temperature. The slight difference between the SCOF-Tol spectra and that of SCOF-Acn-HT is likely attributed to a minor LS contamination due to incomplete SCO.

Evaluating the Fe K-edge XANES spectra, the shift of the white line and pre-edge feature trends are also consistent with the expected spin state and in line with the literature precedent. 30,32,69 The edge shift is associated with changes in Fe-N bond lengths during spin transition, with shorter bond lengths leading to higher edge energy. The pre-edge feature ramifications of different Fe spin state configurations have been thoroughly documented and are well understood through multiplet analysis based on crystal field theory. 48,70 In Fe^{II} d⁶ systems with approximate octahedral symmetry, the LS electron configuration has fully filled t_{2g} orbitals and empty e_g orbitals, yielding a single quadrupole-allowed 1s to 3d(e_g) pre-edge feature, while the partially filled t_{2g} and e_g orbitals of the HS configuration enable excitation to both sets, producing multiple transitions that generally yield two resolved pre-edge features. Furthermore, the TD-DFT calculation results (Figure 5) show this expected d-orbital parentage of the pre-edge features in the simulated spectra. The lowest energy pre-edge features of the SCOF-Acn spectrum demonstrate the anticipated pattern upon temperature-induced spin state change, with SCOF-Acn-HT displaying the two resolved preedge peaks characteristic of the HS state and SCOF-Acn-LT displaying one, indicating LS. Unsurprisingly, the SCOF-Tol system produces the two pre-edge feature signatures for the HS state regardless of temperature. These trends are observed with better resolution in the HERFD-XANES spectra shown in Figure 4. Furthermore, hints of the underlying multiplet features associated with the HS and LS configurations, which remain unresolved in the spectral slices, are observed in the RXES planes (Figure 3 top) and are consistent with observations for other HS and LS Fe systems. 48,70 These pre-edge spectral differences further confirm the spin state status of these SCOFs including the thermally induced HS/LS spin state transition with the acetonitrile guest environment. The Ni K-edge XANES spectra for these systems (Figure S2) are nearly identical, indicating minimal direct electronic interactions between the guest molecules and Ni sites of the SCOF.

Fe K-edge EXAFS analysis (Figure 2) provides additional insight on the spin state status along with attendant structural changes and intrinsic disorder of the SCOF with different solvent guest environments. The Fe–N bond lengths derived from the fits are significantly shorter (by ~0.15 and ~0.27 Å for equatorial and axial bonds, respectively) in the LS system, when compared to the HS systems (Supporting Information Tables S1 and S2), which is in line with the established crystal structures of the HS and LS frameworks¹⁹ as well as previously reported EXAFS studies on related SCO complexes. ^{69,71,72} The reduced amplitude of this first shell peak for the HS SCOF, irrespective of the solvent guest, points to higher disorder of the local Fe site coordination in this spin state regardless of the

framework pore environment. The Fe–Ni scattering path peak is also suppressed for the HS systems, which signals increased disorder within the (a-b) crystallographic plane. Notably, this peak displays significantly more amplitude reduction for the SCOF-Tol system than for SCOF-Acn-HT, suggesting a higher degree of longer-range disorder overall with the toluene guest environment. A similar trend is observed in the Ni EXAFS spectra (Figure S2) which show marked amplitude reduction of the Ni–Fe scattering peak for the HS SCOF systems. Comparison of the SCOF-Tol Fe EXAFS spectra collected at the two temperature extremes (Figure 2) shows negligible differences, consistent with the absence of spin flip. This observation also shows that the Fe spin state rather than the temperature effect alone dictates the observed spectral appearance for these systems.

The EXAFS spectra solvent dependence reveals the influence of the guest species within the framework on the Fe spin state stabilization, as previously hypothesized. 19,24-26,34,35 The acetonitrile guest molecules likely interact with the axially coordinated pyrazine rings' π systems, which effectively stabilizes the LS state at higher temperatures (compared to the toluene guest environment) and allows contraction of the Fe first shell coordination upon HS to LS transition. The SCO occurs without as much change in structural disorder within the Fe-Ni equatorial plane as required under the toluene guest environment. As a larger guest molecule within the pores of the SCOF, toluene hampers this contraction, thereby stabilizing the HS state at ambient temperatures. The more constrained pore environment produced by this solvent however yields increased variance in the Fe-Ni path length and thus increased disorder of the Ni metal centers in this plane.

XANES Edge Features: Assignment and Electronic Structure Insights. Unlike XANES pre-edge features of first-row transition metal systems, higher-energy, bound transitions appearing on the rising edge, while commonly documented, are seldom fully understood. For one, their assignment is often complicated, involving non-local CT transitions with strong neighboring ligand orbital contributions. Furthermore, convolution of features in this region with the rising edge and multiple scattering effects can partially or even completely obscure them. In the SCOF materials studied in this work, edge features are relatively low in energy, allowing HERFD—XANES (Figure 4) to expose the more complicated underlying structure in this edge region that is otherwise obscured by broadening in conventional XANES.

We attempt to assign the orbital parentage of these edge features using ligand field theory arguments aided by TD-DFT calculations. Cyanide is a known π acceptor and a stronger field ligand than pyrazine. Therefore, if the acceptor orbitals associated with the edge features around 7115-7120 eV have both metal d and either cyanide or pyrazine ligand character, then the increased metal contribution resulting from the π back donation to the cyanide ligand portends XAS transitions at higher energy positions relative to those involving pyrazine. The TD-DFT calculation results, shown in Figure 5, further support this edge feature energy ordering. The calculated increase in metal 4p orbital contribution explains the higher relative intensity for the transition involving the cyano ligand. The simulated spectra include transitions in this energy range above the pre-edge that derive from the localized 1s orbital to mixed metal 3d/4p + ligand π^* molecular orbitals (MOs). The less intense, lower-energy shoulder features arise from

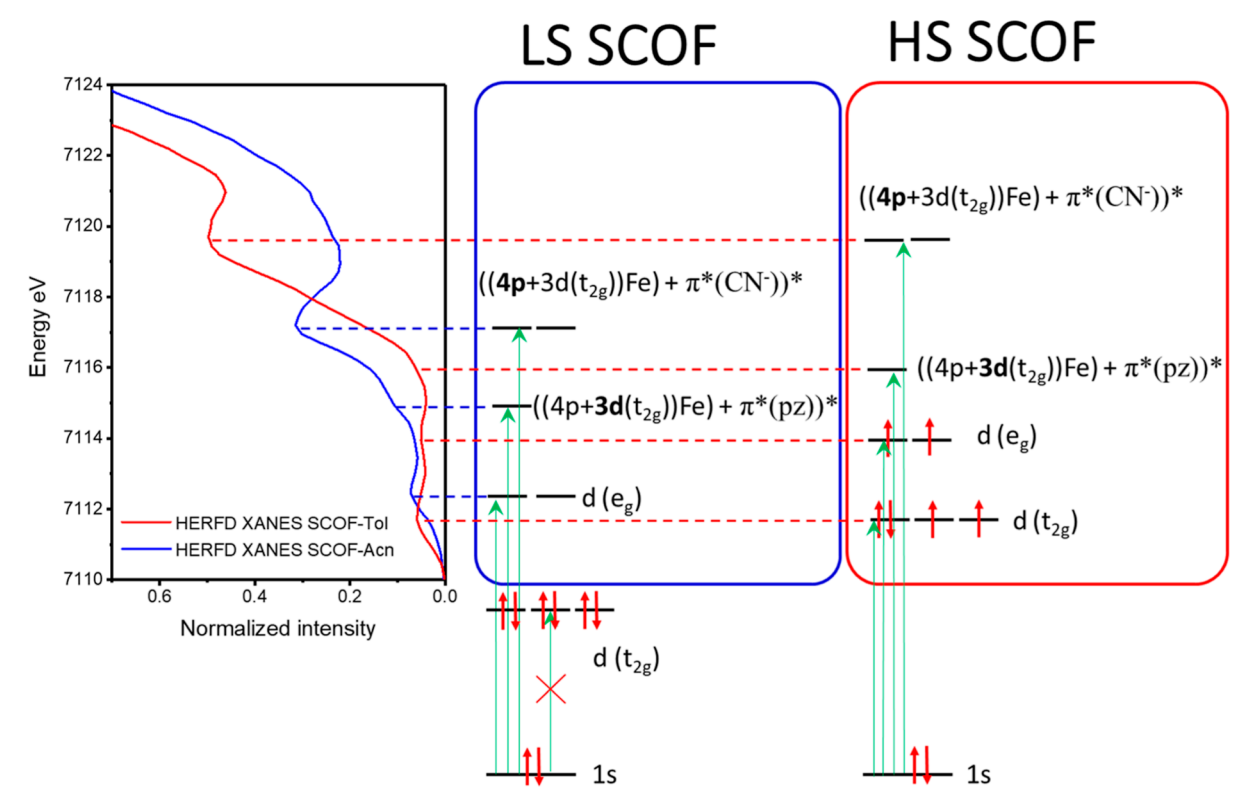


Figure 6. MO diagram of LS and HS SCOF systems with accompanying assignments of pre-edge and edge features of the Fe K-edge HERFD—XANES spectra rotated and shown on the left. Dominant atomic orbital contribution indicated in bold.

transitions involving acceptor orbitals with the prevailing π^* electron density on the pyrazine ligands, while the more intense, higher-energy features correspond to analogous CT transitions with the acceptor orbitals instead dominated by the cyano π^* electron density and increased metal 4p contribution. These assignments are summarized in Figure 6, which shows the proposed MO diagram, truncated to the valence orbital region (the expanded MO diagram is shown in Figure S7). Here, the 1s \rightarrow 3d/4p + π^* (pz) and 1s \rightarrow 3d/4p + π^* (CN) transitions are depicted along with the localized 1s \rightarrow 3d transitions in connections with the corresponding edge and pre-edge features observed in the HERFD-XANES spectra. Notably, these edge feature assignments are consistent with those made for a related Fe(II) complex with strong π -back bonding ligands, ferrocyanide, which were based on similar studies using K α RXES.⁵³

Given the underlying ligand participation, the behavior of these edge-transition features upon SCO directly reflects the electronic structure changes of the corresponding Fe-L bonds. The change from LS to HS results in both edge features shifting to higher energy. The smaller d-orbital splitting in the HS state effectively increases the energy of the associated acceptor orbitals and therefore the corresponding 1s transition energies. Since the Fe-L bonds elongate in the process, the overlap between ligand π^* and metal d orbitals decreases. For the cyano ligands with strong π -back bonding, this has a significant impact on the intensity of the associated 1s transition, which becomes more localized and dipole-allowed due to the reduced CT character and increased contribution of local metal 4p character in the acceptor states. This intensity trend for the resolved 1s \rightarrow 3d/4p + π^* (CN) edge feature is confirmed by the edge-subtracted HERFD-XANES spectra (Figure S11) as well as the TD-DFT calculations (Figure 5,

Tables S4 and S6), which reveal an overall higher metal 4p contribution to the set of acceptor orbitals. These observations indicate lower covalency of the Fe—cyano bonds in the HS state. The analogous assessment of the Fe—pyrazine bond covalency upon LS \rightarrow HS transition is less clear because the associated XAS edge feature has much lower intensity overall and is therefore poorly resolved, particularly in the HS systems. TD-DFT calculations, however, predict a far less drastic change in intensity for the corresponding transitions, which appears to be matched experimentally. The $\pi^*(pz)$ acceptor orbitals are predicted to have higher relative metal 3d versus 4p atomic orbital contribution. Structural changes that would alter the metal 4p character (and therefore the dipole contribution to the transition oscillator strength) would have less effect on the intensity.

2D RXES Analysis: Spin-Selective Resonance Behavior of Localized and Delocalized XAS Transitions. The $K\beta_{1,3}$ and $K\beta'$ emission resonance behavior observed in the 2D RXES planes and the corresponding CEE slices (Figure 3) reflects the spin selectivity of the localized $1s \rightarrow 3d$ pre-edge features. While all three SCOF systems display pre-edge feature resonances with the $K\beta_{13}$ emission peak (7057–7058 eV), only the LS system, SCOF-Acn-LT, also exhibits $K\beta'$ emission resonance (around 7041 eV) for its pre-edge transition band. This resonance behavior derives from the delectron configuration in the two spin states shown in Figure 6. The LS d^6 electron configuration has empty $d(e_g)$ orbitals that can accept electrons of either spin parity upon core excitation. Therefore, the $K\beta$ decay can occur for either spin as well, generating a pre-edge feature in resonance with both $K\beta_{1,3}$ and $K\beta'$ emission peaks. For HS systems, on the other hand, with both sets of d orbitals at least partially occupied, only mainline $K\beta$ resonance is observed since only one spin parity can be

promoted to the d shell (and therefore decay via $K\beta$ emission). The broad background intensity observed in the pre-edge region of the CEE slice for these HS systems stems from the interference with the $\Gamma_{\rm int}$ broadening feature (highlighted by the diagonal dashed line superimposed on the corresponding RXES planes in Figure 3) that extends into this energy range.

The resonance behavior of the higher-energy XANES edge features further supports their non-local CT character assignment as described above. With significant ligand contribution to the acceptor orbitals associated with these transitions, the resulting delocalization should allow 1s excitation of either spin state and thus also decay via both $K\beta_{1,3}$ and $K\beta'$ emission channels. For the HS systems, the main edge feature [assigned to 1s \rightarrow 3d/4p+ π *(CN)] resonances with both $K\beta_{1,3}$ and $K\beta'$ are indeed clearly seen in the 2D spectra and the corresponding CEE slices (Figure 3). The LS SCOF displays analogous spin state-independent resonance behavior of its edge feature as well, although with some degree of ambiguity. $K\beta_{1,3}$ resonance is distinctly observed in the 2D RXES spectra and the corresponding CEE slice taken at 7055 eV. $K\beta'$ resonance, however, overlaps strongly with the $\Gamma_{\rm int}$ broadening feature that spreads into this energy range. Despite this interference, $K\beta'$ resonance is nonetheless suggested by the small feature protruding from this background intensity around 7117 eV in the CEE slice collected at 7041 eV. The lower-energy edge feature shoulder assigned to 1s \rightarrow 4p/3d + $\pi^*(pz)$ for both HS and LS systems is too weak and unresolved to confidently assess any resonance behavior. However, given the pyrazine ligand acceptor orbital contribution, the resulting delocalization would also predict spin state insensitivity of its emission band resonance.

CONCLUSIONS

Metal K-edge X-ray spectroscopy methods were used to probe the guest-dependent SCO behavior of the $Fe^{II}(pz)[Ni^{II}(CN)_4]$ Hofmann-type 3D lattice. Beyond the in situ confirmation of the thermally induced spin state change, $K\beta$ RXES allowed us to resolve the XANES edge feature transitions and, in combination with the TD-DFT calculations, confidently assign their orbital parentage. Analysis of the full RXES planes as opposed to conventional XANES or even simply 1D HERFD-XANES slices was crucial to the accurate interpretation of preedge and edge feature resonance patterns in the presence of other overlapping broadening contributors to observed intensity in this region. With knowledge of the ligand contributions, we could then connect the edge feature behavior to the specific metal-ligand bond covalency changes accompanying the spin transition. The hard X-ray K β RXES method applied to the iron-based SCOF materials in this study demonstrated its capacity for providing dual electronic structure insights on both metal spin and bond covalency under controlled sample environments.

ASSOCIATED CONTENT

Supporting Information

The Supporting Information is available free of charge at https://pubs.acs.org/doi/10.1021/acs.inorgchem.2c00774.

PXRD characterization data, conventional Ni K-edge X-ray absorption data, additional Fe K-edge X-ray absorption and HERFD-XANES spectra, Fe $K\beta$ energy transfer RIXS plots, expanded MO diagrams, additional

information on the EXAFS fitting model and results, and details on TD-DFT calculations (PDF)

AUTHOR INFORMATION

Corresponding Author

Jenny V. Lockard — Department of Chemistry, Rutgers University—Newark, Newark, New Jersey 07102, United States; orcid.org/0000-0001-7758-169X; Email: jlockard@newark.rutgers.edu

Authors

Mikhail Solovyev — Department of Chemistry, Rutgers University—Newark, Newark, New Jersey 07102, United States

Pavel Kucheryavy — Department of Chemistry, Rutgers University—Newark, Newark, New Jersey 07102, United States

Complete contact information is available at: https://pubs.acs.org/10.1021/acs.inorgchem.2c00774

Notes

The authors declare no competing financial interest.

ACKNOWLEDGMENTS

This material is based upon work supported by the National Science Foundation under grant no. DMR-2003910. This research used resources of the Advanced Photon Source, an Office of Science User Facility operated for the U.S. Department of Energy (DOE) Office of Science by Argonne National Laboratory, and was supported by the U.S. DOE under contract no. DE-AC02-06CH11357 and the Canadian Light Source and its funding partners. The authors acknowledge the Office of Advanced Research Computing (OARC) at Rutgers, the State University of New Jersey for providing access to the Amarel cluster, and associated research computing resources that have contributed to the results reported here. URL: https://it.rutgers.edu/oarc.

REFERENCES

- (1) Rubio-Giménez, V. .; Tatay, S.; Martí-Gastaldo, C. Electrical conductivity and magnetic bistability in metal—organic frameworks and coordination polymers: charge transport and spin crossover at the nanoscale. *Chem. Soc. Rev.* **2020**, *49*, 5601–5638.
- (2) Muñoz, M. C.; Real, J. A. Thermo-, piezo-, photo- and chemoswitchable spin crossover iron(II)-metallocyanate based coordination polymers. *Coord. Chem. Rev.* **2011**, 255, 2068–2093.
- (3) Otsubo, K.; Haraguchi, T.; Kitagawa, H. Nanoscale crystalline architectures of Hofmann-type metal—organic frameworks. *Coord. Chem. Rev.* **2017**, 346, 123–138.
- (4) Cui, Y.; Li, B.; He, H.; Zhou, W.; Chen, B.; Qian, G. Metal—Organic Frameworks as Platforms for Functional Materials. *Acc. Chem. Res.* **2016**, 49, 483–493.
- (5) Furukawa, H.; Cordova, K. E.; O'Keeffe, M.; Yaghi, O. M. The Chemistry and Applications of Metal-Organic Frameworks. *Science* **2013**, *341*, 1230444.
- (6) Wang, C.; Liu, D.; Lin, W. Metal-Organic Frameworks as A Tunable Platform for Designing Functional Molecular Materials. *J. Am. Chem. Soc.* **2013**, *135*, 13222–13234.
- (7) Foo, M. L.; Matsuda, R.; Kitagawa, S. Functional Hybrid Porous Coordination Polymers. *Chem. Mater.* **2014**, *26*, 310–322.
- (8) Hu, Z.; Deibert, B. J.; Li, J. Luminescent metal-organic frameworks for chemical sensing and explosive detection. *Chem. Soc. Rev.* **2014**, *43*, 5815–5840.
- (9) Yuan, S.; Feng, L.; Wang, K.; Pang, J.; Bosch, M.; Lollar, C.; Sun, Y.; Qin, J.; Yang, X.; Zhang, P.; Wang, Q.; Zou, L.; Zhang, Y.; Zhang,

- L.; Fang, Y.; Li, J.; Zhou, H. C. Stable Metal-Organic Frameworks: Design, Synthesis, and Applications. *Adv. Mater.* **2018**, *30*, 1704303.
- (10) Meng, Y.; Dong, Y.-J.; Yan, Z.; Chen, Y.-C.; Song, X.-W.; Li, Q.-W.; Zhang, C.-L.; Ni, Z.-P.; Tong, M.-L. A New Porous Three-Dimensional Iron(II) Coordination Polymer with Solvent-Induced Reversible Spin-Crossover Behavior. *Cryst. Growth Des.* **2018**, *18*, 5214–5219.
- (11) Murphy, M. J.; Zenere, K. A.; Ragon, F.; Southon, P. D.; Kepert, C. J.; Neville, S. M. Guest Programmable Multistep Spin Crossover in a Porous 2-D Hofmann-Type Material. *J. Am. Chem. Soc.* **2017**, *139*, 1330–1335.
- (12) Neville, S. M.; Halder, G. J.; Chapman, K. W.; Duriska, M. B.; Moubaraki, B.; Murray, K. S.; Kepert, C. J. Guest Tunable Structure and Spin Crossover Properties in a Nanoporous Coordination Framework Material. *J. Am. Chem. Soc.* **2009**, *131*, 12106–12108.
- (13) Bartual-Murgui, C.; Akou, A.; Shepherd, H. J.; Molnár, G.; Real, J. A.; Salmon, L.; Bousseksou, A. Tunable Spin-Crossover Behavior of the Hofmann-like Network {Fe(bpac)[Pt(CN)4]} through Host—Guest Chemistry. *Chem.—Eur. J.* **2013**, *19*, 15036—15043.
- (14) Halder, G. J.; Kepert, C. J.; Moubaraki, B.; Murray, K. S.; Cashion, J. D. Guest-Dependent Spin Crossover in a Nanoporous Molecular Framework Material. *Science* **2002**, *298*, 1762–1765.
- (15) Aravena, D.; Castillo, Z. A.; Muñoz, M. C.; Gaspar, A. B.; Yoneda, K.; Ohtani, R.; Mishima, A.; Kitagawa, S.; Ohba, M.; Real, J. A.; Ruiz, E. Guest Modulation of Spin-Crossover Transition Temperature in a Porous Iron(II) Metal—Organic Framework: Experimental and Periodic DFT Studies. *Chem.—Eur. J.* **2014**, *20*, 12864—12873.
- (16) Deshmukh, M. M.; Ohba, M.; Kitagawa, S.; Sakaki, S. Shigeyoshi; Absorption of CO2 and CS2 into the Hofmann-Type Porous Coordination Polymer: Electrostatic versus Dispersion Interactions. J. Am. Chem. Soc. 2013, 135, 4840–4849.
- (17) Arcís-Castillo, Z.; Francisco, J.; Muñoz, M. C.; Aravena, D.; Gaspar, A. B.; Sánchez-Royo; Juan, F.; Ruiz, E.; Ohba, M.; Matsuda, R.; Kitagawa, S.; Real, J. A. Reversible Chemisorption of Sulfur Dioxide in a Spin Crossover Porous Coordination Polymer. *Inorg. Chem.* **2013**, *52*, 12777–12783.
- (18) Polyzou, C. D.; Lalioti, N.; Psycharis, V.; Tangoulis, V. Guest induced hysteretic tristability in 3D pillared Hofmann-type microporous metal—organic frameworks. *New J. Chem.* **2017**, *41*, 12384—12387.
- (19) Southon, P. D.; Liu, L.; Fellows, E. A.; Price, D. J.; Halder, G. J.; Chapman, K. W.; Moubaraki, B.; Murray, K. S.; Létard, J.-F.; Kepert, C. J. Dynamic Interplay between Spin-Crossover and Host—Guest Function in a Nanoporous Metal—Organic Framework Material. J. Am. Chem. Soc. 2009, 131, 10998—11009.
- (20) Boldog, I.; Gaspar, A. B.; Martínez, V.; Pardo-Ibañez, P.; Ksenofontov, V.; Bhattacharjee, A.; Gütlich, P.; Real, J. A. Spin-Crossover Nanocrystals with Magnetic, Optical, and Structural Bistability Near Room Temperature. *Angew. Chem., Int. Ed.* **2008**, 47, 6433–6437.
- (21) Ohba, M.; Yoneda, K.; Agustí, G.; Muñoz, M. C.; Gaspar, A. B.; Real, J. A.; Yamasaki, M.; Ando, H.; Nakao, Y.; Sakaki, S.; Kitagawa, S. Susumu; Bidirectional Chemo-Switching of Spin State in a Microporous Framework. *Angew. Chem., Int. Ed.* **2009**, 48, 4767–4771.
- (22) Niel, V.; Martinez-Agudo, J. M.; Muñoz, M. C.; Gaspar, A. B.; Real, J. A.; Real, J. A. Cooperative Spin Crossover Behavior in Cyanide-Bridged Fe(II)–M(II) Bimetallic 3D Hofmann-like Networks (M = Ni, Pd, and Pt). *Inorg. Chem.* **2001**, *40*, 3838–3839.
- (23) Clements, J. E.; Price, J. R.; Neville, S. M.; Kepert, C. J. Hysteretic Four-Step Spin Crossover within a Three-Dimensional Porous Hofmann-like Material. *Angew. Chem., Int. Ed.* **2016**, 55, 15105–15109.
- (24) Cirera, J.; Babin, V.; Paesani, F. Theoretical Modeling of Spin Crossover in Metal—Organic Frameworks: [Fe(pz)2Pt(CN)4] as a Case Study. *Inorg. Chem.* **2014**, *53*, 11020—11028.
- (25) Pham, C. H.; Cirera, J.; Paesani, F. Molecular Mechanisms of Spin Crossover in the {Fe(pz)[Pt(CN)4]} Metal-Organic Frame-

- work upon Water Adsorption. J. Am. Chem. Soc. 2016, 138, 6123-6126.
- (26) Muñoz Lara, F. J.; Gaspar, A. B.; Aravena, D.; Ruiz, E.; Muñoz, M. C.; Ohba, M.; Ohtani, R.; Kitagawa, S.; Real, J. A.; Real, J. A. Enhanced bistability by guest inclusion in Fe(ii) spin crossover porous coordination polymers. *Chem. Commun.* **2012**, *48*, 4686–4688.
- (27) Molnár, G. .; Rat, S.; Salmon, L.; Nicolazzi, W.; Bousseksou, A. Spin Crossover Nanomaterials: From Fundamental Concepts to Devices. *Adv. Mater.* **2018**, *30*, 1703862.
- (28) Molnár, G.; Mikolasek, M.; Ridier, K.; Fahs, A.; Nicolazzi, W.; Bousseksou, A. Molecular Spin Crossover Materials: Review of the Lattice Dynamical Properties. *Ann. Phys.* **2019**, *531*, 1900076.
- (29) Ueno, S.; Kawasaki, T.; Okabayashi, J.; Kitazawa, T. Structural, Electronic, and Magnetic Properties of Novel Spin-Crossover Complex: Fe(butyl nicotinate)2[Au(CN)2]2. *Bull. Chem. Soc. Jpn.* **2015**, *88*, 551–553.
- (30) Okabayashi, J.; Ueno, S.; Kawasaki, T.; Kitazawa, T. Ligand 4-X pyridine (X=Cl, Br, I) dependence in Hofmann-type spin crossover complexes: Fe(4-Xpyridine)2[Au(CN)2]2. *Inorg. Chim. Acta* **2016**, 445, 17–21.
- (31) Mohamed, A.; Lee, M.; Kitase, K.; Kitazawa, T.; Kim, J.-Y.; Cho, D.-Y. Soft X-ray Absorption Spectroscopy Study of Spin Crossover Fe-Compounds: Persistent High Spin Configurations under Soft X-ray Irradiation. *Crystals* **2018**, *8*, 433.
- (32) Kitase, K.; Kitazawa, T. A novel two-step Fe—Au type spin-crossover behavior in a Hofmann-type coordination complex {Fe(4-methylpyrimidine)2[Au(CN)2]2. *Dalton Trans.* **2020**, *49*, 12210–12214.
- (33) Kitase, K.; Akahoshi, D.; Kitazawa, T. Effects of Both Methyl and Pyrimidine Groups in Fe–Ag Spin-Crossover Hofmann-Type Complex {Fe(4-Methylpyrimidine)2[Ag(CN)2]2. *Inorg. Chem.* **2021**, 60, 4717–4722.
- (34) Ando, H.; Nakao, Y.; Sato, H.; Ohba, M.; Kitagawa, S.; Sakaki, S. Theoretical study on high-spin to low-spin transition of {Fe(pyrazine)[Pt(CN)4]}: Guest-induced entropy decrease. *Chem. Phys. Lett.* **2011**, *511*, 399–404.
- (35) Pham, C. H.; Paesani, F. Guest-Dependent Stabilization of the Low-Spin State in Spin-Crossover Metal-Organic Frameworks. *Inorg. Chem.* **2018**, *57*, 9839–9843.
- (36) Kitazawa, T.; Gomi, Y.; Takahashi, M.; Takeda, M.; Enomoto, M.; Miyazaki, A.; Enoki, T. Spin-crossover behaviour of the coordination polymer FeII(C5H5N)2NiII(CN)4. *J. Mater. Chem.* **1996**, *6*, 119–121.
- (37) Kitazawa, T.; Kawasaki, T.; Shiina, H.; Takahashi, M.; Mossbauer Spectroscopic Study on Hofmann-like Coordination Polymer Fe[(4-Clpy).sub.2][Ni[(CN).sub.4]]. *Croat. Chem. Acta* **2016**, 89, 111–115. DOI: 10.5562/cca2758
- (38) Kitazawa, T.; Kishida, T.; Kawasaki, T.; Takahashi, M. Spin crossover behaviour in Hofmann-like coordination polymer Fe(py)-2[Pd(CN)4] with 57Fe Mössbauer spectra. *Hyperfine Interact.* **2017**, 238, 65.
- (39) Chorazy, S.; Charytanowicz, T.; Pinkowicz, D.; Wang, J.; Nakabayashi, K.; Klimke, S.; Renz, F.; Ohkoshi, S. i.; Sieklucka, B. Octacyanidorhenate(V) Ion as an Efficient Linker for Hysteretic Two-Step Iron(II) Spin Crossover Switchable by Temperature, Light, and Pressure. Angew. Chem., Int. Ed. 2020, 59, 15741–15749.
- (40) Gamblin, S. D.; Urch, D. S. Metal K β X-ray Emission Spectra of First Row Transition Metal Compounds. *J. Electron Spectrosc. Relat. Phenom.* **2001**, *113*, 179–192.
- (41) Bergmann, U.; Glatzel, P.; Robblee, J. H.; Messinger, J.; Fernandez, C.; Cinco, R.; Visser, H.; McFarlane, K.; Bellacchio, E.; Pizarro, S.; Sauer, K.; Yachandra, V. K.; Klein, M. P.; Cox, B. L.; Nealson, K. H.; Cramer, S. P. High-resolution X-ray Spectroscopy of Rare Events: A Different Look at Local Structure and Chemistry. *J. Synchrotron Radiat.* **2001**, *8*, 199–203.
- (42) Eisenberger, P.; Platzman, P. M.; Winick, H. X.-Ray Resonant Raman Scattering: Observation of Characteristic Radiation Narrower than the Lifetime Width. *Phys. Rev. Lett.* **1976**, *36*, 623–626.

- (43) Safonova, O. V.; Tromp, M.; van Bokhoven, J. A.; de Groot, F. M. F.; Evans, J.; Glatzel, P.; Evans, J.; Glatzel, P. Identification of CO Adsorption Sites in Supported Pt Catalysts Using High-Energy-Resolution Fluorescence Detection X-ray Spectroscopy. *J. Phys. Chem. B* **2006**, *110*, 16162—16164.
- (44) Atkins, A. J.; Bauer, M.; Jacob, C. R. High-resolution X-ray absorption spectroscopy of iron carbonyl complexes. *Phys. Chem. Chem. Phys.* **2015**, *17*, 13937–13948.
- (45) Glatzel, P.; Sikora, M.; Fernández-García, M. Resonant X-ray spectroscopy to study K absorption pre-edges in 3d transition metal compounds. *Eur. Phys. J. Spec. Top.* **2009**, *169*, 207–214.
- (46) Rueff, J.-P.; Journel, L.; Petit, P.-E.; Farges, F. Fe K pre-edges as revealed by resonant x-ray emission. *Phys. Rev. B: Condens. Matter Mater. Phys.* **2004**, *69*, 235107.
- (47) Glatzel, P.; Bergmann, U.; Yano, J.; Visser, H.; Robblee, J. H.; Gu, W.; de Groot, F. M. F.; Christou, G.; Pecoraro, V. L.; Cramer, S. P.; Yachandra, V. K.; Yachandra, V. K. The Electronic Structure of Mn in Oxides, Coordination Complexes, and the Oxygen-Evolving Complex of Photosystem II Studied by Resonant Inelastic X-ray Scattering. *J. Am. Chem. Soc.* **2004**, *126*, 9946–9959.
- (48) Vankó, G.; Neisius, T.; Molnár, G. .; Renz, F.; Kárpáti, S.; Shukla, A.; de Groot; Frank, M. F. Probing the 3d Spin Momentum with X-ray Emission Spectroscopy: The Case of Molecular-Spin Transitions. *J. Phys. Chem. B* **2006**, *110*, 11647–11653.
- (49) Yamaoka, H.; Oura, M.; Taguchi, M.; Morikawa, T.; Takahiro, K.; Terai, A.; Kawatsura, K.; Mukoyama, T.; Mukoyama, T. $K\beta$ Resonant X-ray Emission Spectroscopy for Fe, Fe2O3 and Fe3O4. *J. Phys. Soc. Jpn.* **2004**, *73*, 3182–3191.
- (50) Glatzel, P.; Mirone, A.; Eeckhout, S. G.; Sikora, M.; Giuli, G. Orbital hybridization and spin polarization in the resonant 1s photoexcitations of alpha-Fe2O3. *Phys. Rev. B: Condens. Matter Mater. Phys.* **2008**, *77*, 115133.
- (51) Vankó, G.; Bordage, A.; Glatzel, P.; Gallo, E.; Rovezzi, M.; Gawelda, W.; Galler, A.; Bressler, C.; Doumy, G.; March, A. M.; Kanter, E. P.; Young, L.; Southworth, S. H.; Canton, S. E.; Uhlig, J.; Smolentsev, G.; Sundström, V.; Haldrup, K.; Nielsen, M. M.; Kjaer, K. S.; Lemke, H. T. Spin-state studies with XES and RIXS: From static to ultrafast. *J. Electron Spectrosc. Relat. Phenom.* **2013**, 188, 166–171.
- (52) Glatzel, P.; Bergmann, U. High Resolution 1s Core Hole X-ray Spectroscopy in 3d Transition Metal Complexes—Electronic and Structural information. *Coord. Chem. Rev.* **2005**, 249, 65–95.
- (53) Lundberg, M.; Kroll, T.; DeBeer, S.; Bergmann, U.; Wilson, S. A.; Glatzel, P.; Nordlund, D.; Hedman, B.; Hodgson, K. O.; Solomon, E. I. Metal—Ligand Covalency of Iron Complexes from High-Resolution Resonant Inelastic X-ray Scattering. *J. Am. Chem. Soc.* **2013**, *135*, 17121–17134.
- (54) Hocking, R. K.; George, S. D.; Raymond, K. N.; Hodgson, K. O.; Hedman, B.; Solomon, E. I. Fe L-Edge X-ray Absorption Spectroscopy Determination of Differential Orbital Covalency of Siderophore Model Compounds: Electronic Structure Contributions to High Stability Constants. J. Am. Chem. Soc. 2010, 132, 4006–4015.
- (55) Wilson, S. A.; Kroll, T.; Decreau, R. A.; Hocking, R. K.; Lundberg, M.; Hedman, B.; Hodgson, K. O.; Solomon, E. I. Iron L-Edge X-ray Absorption Spectroscopy of Oxy-Picket Fence Porphyrin: Experimental Insight into Fe-O2 Bonding. *J. Am. Chem. Soc.* **2013**, 135, 1124–1136.
- (56) Hocking, R. K.; Wasinger, E. C.; Yan, Yi-L.; deGroot, F. M. F.; Walker, F. A.; Hodgson, K. O.; Hedman, B.; Solomon, E. I. Fe L-Edge X-ray Absorption Spectroscopy of Low-Spin Heme Relative to Nonheme Fe Complexes: Delocalization of Fe d-Electrons into the Porphyrin Ligand. J. Am. Chem. Soc. 2007, 129, 113–125.
- (57) Wasinger, E. C.; de Groot, F. M. F.; Hedman, B.; Hodgson, K. O.; Solomon, E. I.; Solomon, E. I. L-edge X-ray Absorption Spectroscopy of Non-Heme Iron Sites: Experimental Determination of Differential Orbital Covalency. *J. Am. Chem. Soc.* **2003**, *125*, 12894–12906.
- (58) Baker, M. L.; Mara, M. W.; Yan, J. J.; Hodgson, K. O.; Hedman, B.; Solomon, E. I. K.- and L.-edge X-ray absorption spectroscopy (XAS) and resonant inelastic X-ray scattering (RIXS) determination

- of differential orbital covalency (DOC) of transition metal sites. *Coord. Chem. Rev.* **2017**, *345*, 182–208.
- (59) Solomon, E. I.; Hedman, B.; Hodgson, K. O.; Dey, A.; Szilagyi, R. K. Ligand K-edge X-ray absorption spectroscopy: covalency of ligand—metal bonds. *Coord. Chem. Rev.* **2005**, 249, 97–129.
- (60) Ravel, B.; Newville, M. ATHENA, ARTEMIS, HEPHAESTUS: Data Analysis for X-ray Absorption Spectroscopy Using IFEFFIT. *J. Synchrotron Radiat.* **2005**, *12*, 537–541.
- (61) Mattern, B. A.; Seidler, G. T.; Haave, M.; Pacold, J. I.; Gordon, R. A.; Planillo, J.; Quintana, J.; Rusthoven, B. A plastic miniature x-ray emission spectrometer based on the cylindrical von Hamos geometry. *Rev. Sci. Instrum.* **2012**, *83*, 023901.
- (62) Neese, F. *The ORCA Program System*; Wiley Interdiscip Rev Comput Mol Sci, 2012; Vol. 2, pp 73–78.
- (63) Adamo, C.; Barone, V. Toward reliable density functional methods without adjustable parameters: The PBE0 model. *J. Chem. Phys.* **1999**, *110*, 6158–6170.
- (64) Pantazis, D. A.; Chen, X.-Y.; Landis, C. R.; Neese, F. All-Electron Scalar Relativistic Basis Sets for Third-Row Transition Metal Atoms. *J. Chem. Theory Comput.* **2008**, *4*, 908–919.
- (65) Neese, F. Prediction and interpretation of the 57Fe isomer shift in MA¶ssbauer spectra by density functional theory. *Inorg. Chim. Acta* **2002**, 337, 181–192.
- (66) van Lenthe, E.; van der Avoird, A.; Wormer, P. E. S. Density functional calculations of molecular hyperfine interactions in the zero order regular approximation for relativistic effects. *J. Chem. Phys.* **1998**, *108*, 4783–4796.
- (67) Klamt, A.; Schüürmann, G. COSMO: a new approach to dielectric screening in solvents with explicit expressions for the screening energy and its gradient. *J. Chem. Soc., Perkin Trans.* 2 **1993**, 799–805.
- (68) DeBeer George, S.; Petrenko, T.; Neese, F. Time-dependent density functional calculations of ligand K-edge X-ray absorption spectra. *Inorg. Chim. Acta* **2008**, *361*, 965–972.
- (69) Seredyuk, M.; Gaspar, A. B.; Ksenofontov, V.; Verdaguer, M.; Villain, F.; Gütlich, P. Thermal- and Light-Induced Spin Crossover in Novel 2D Fe(II) Metalorganic Frameworks {Fe(4-PhPy)2[MII(CN)-x]y}·sH2O: Spectroscopic, Structural, and Magnetic Studies. *Inorg. Chem.* **2009**, *48*, 6130–6141.
- (70) Westre, T. E.; Kennepohl, P.; DeWitt, J. G.; Hedman, B.; Hodgson, K. O.; Solomon, E. I. A Multiplet Analysis of Fe K-Edge 1s → 3d Pre-Edge Features of Iron Complexes. *J. Am. Chem. Soc.* **1997**, 119, 6297–6314.
- (71) Okabayashi, J.; Ueno, S.; Wakisaka, Y.; Kitazawa, T. Temperature-dependent EXAFS study for spin crossover complex: Fe(pyridine)2Ni(CN)4. *Inorg. Chim. Acta* **2015**, 426, 142–145.
- (72) Rudd, D. J.; Goldsmith, C. R.; Cole, A. P.; Stack, T. D. P.; Hodgson, K. O.; Hedman, B. X-ray Absorption Spectroscopic Investigation of the Spin-Transition Character in a Series of Single-Site Perturbed Iron(II) Complexes. *Inorg. Chem.* 2005, 44, 1221–1229